1 2 3 4	Fiber Engagement Accounts For Geometry-Dependent Annulus Fibrosus Mechanics: A Multiscale, Structure-Based Finite Element Study					
5	Minhao Zhou ¹					
6	Benjamin Werbner ¹					
7	Grace D. O'Connell ^{1,2}					
8						
9	¹ Department of Mechanical Engineering					
10	University of California, Berkeley, USA					
11	² Department of Orthopaedic Surgery					
12	University of California, San Francisco, USA					
13						
14						
15						
16						
17						
18						
19	Submitted to: Journal of the Mechanical Behavior of Biomedical Materials					
20	Corresponding Author: Grace D. O'Connell					
21	5122 Etcheverry Hall, #1740,					
22	Berkeley, CA, 94720-1740					
23	Phone: 510-642-3739					
24	Fax: 510-643-5539					
25	e-mail: g.oconnell@berkeley.edu					

Abstract

26

27

28

29

30

31

32

33

34

35

36

37

38

39

40

41

42

43

44

45

46

47

48

A comprehensive understanding of biological tissue mechanics is crucial for designing engineered tissues that aim to recapitulate native tissue behavior. Tensile mechanics of many fiberreinforced tissues have been shown to depend on specimen geometry, which makes it challenging to compare data between studies. In this study, a validated multiscale, structure-based finite element model was used to evaluate the effect of specimen geometry on multiscale annulus fibrosus tensile mechanics through a fiber engagement analysis. The relationships between specimen geometry and modulus, Poisson's ratio, tissue stress-strain distributions, and fiber reorientation behaviors were investigated at both tissue and sub-tissue levels. It was observed that annulus fibrosus tissue level tensile properties and stress transmission mechanisms were dependent on specimen geometry. The model also demonstrated that the contribution of fiber-matrix interactions to tissue mechanical response was specimen size- and orientation- dependent. The results of this study reinforce the benefits of structure-based finite element modeling in studies investigating multiscale tissue mechanics. This approach also provides guidelines for developing optimal combined computational-experimental study designs for investigating fiber-reinforced biological tissue mechanics. Additionally, findings from this study help explain the geometry dependence of annulus fibrosus tensile mechanics previously reported in the literature, providing a more fundamental and comprehensive understanding of tissue mechanical behavior. In conclusion, the methods presented here can be used in conjunction with experimental tissue level data to simultaneously investigate tissue and sub-tissue scale mechanics, which is important as the field of soft tissue biomechanics advances toward studies that focus on diminishing length scales. **Keywords:** Annulus fibrosus; Fiber-reinforced angle-ply composites; Geometry dependence; Fiber engagement; Finite element modeling; Multiscale modeling; Structure-based modeling

1. Introduction

49

50

51

52

53

54

55

56

57

58

59

60

61

62

63

64

65

66

67

68

69

70

71

Fiber-reinforced biological tissues are complex composite structures consisting of collagen fibers embedded in a hydrated extrafibrillar matrix, resulting in excellent load-bearing and energy absorption capabilities. A comprehensive understanding of fiber-reinforced tissue mechanics is important for developing tissue repair strategies that recapitulate healthy native tissue mechanical behavior (Long et al. 2016; O'Connell et al. 2015). Previous studies, as well as work within our lab, have suggested that differences in test-specimen geometry may lead to significant differences in tissue-level tensile mechanics, particularly in tissues with fibers oriented off-axis from the applied loading direction (e.g. annulus fibrosus (AF) and meniscus; Adams and Green 1993; Lechner et al. 2000; Werbner et al. 2017). Unfortunately, the large variability of reported values in the literature makes it impossible to directly attribute differences in mechanics between studies to differences in specimen geometry (coefficient of variation for healthy human anterior AF: 0.56– 0.82; Acaroglu et al. 1995; Elliott and Setton 2001; Guerin and Elliott 2006; O'Connell et al. 2009; Żak and Pezowicz 2013; Żak and Pezowicz 2016). This may in part be due to limited tissue availability hindering the development of standardized mechanical testing protocols for fiberreinforced biological tissues (Werbner et al. 2017). Thus, in many cases, it remains unclear whether variations in reported mechanical properties arise from inconsistent experimental protocols (e.g. specimen geometry, boundary conditions, etc.) or structural and compositional changes. Previous investigators hypothesized that variations in specimen geometry alter fiber

Previous investigators hypothesized that variations in specimen geometry alter fiber engagement during loading, resulting in variations in AF tensile modulus (Adams and Green 1993). Adams and Green (1993) used a mathematical model developed based on specimen geometry to show that wider specimens have more engaged fibers during testing, resulting in larger measured modulus values. However, this model was only validated for AF specimens with a fixed length

that were loaded along the axial direction. It was also not capable of examining fiber stress or strain distributions, which were strongly associated with fiber engagement and fiber-matrix interactions (Adams and Green 1993). Subsequent studies using constitutive models demonstrated the contribution of fiber-matrix interactions to AF tensile mechanics (Klisch and Lotz 1999; Elliott and Setton 2001; Guerin and Elliott 2007; O'Connell et al. 2009; O'Connell et al. 2012; Wagner and Lotz 2004; Wagner et al. 2006). However, many of these models were validated using a two-dimensional framework, where hypothesized invariant terms were often physiologically irrelevant and difficult to compare across studies (Guo et al. 2012; Eskandari et al. 2019; Zhou et al. 2020). Predicting tissue mechanics using composite-based frameworks is also limited by tissue heterogeneity, nonlinearity, as well as challenges in experimentally characterizing the structure and mechanics of individual tissue subcomponents (Eberlein et al. 2001; Spilker et al. 1986).

Thus, many researchers have turned to finite element models (FEMs), which can provide three-dimensional predictions of stress—strain distributions throughout fiber-reinforced tissues. In our previous work, a series of FEMs were created based on homogenization theory to guide the development of a robust protocol for AF tensile failure testing (Werbner et al. 2017). This work reported the geometry dependence of AF tensile mechanics, which was accurately replicated by the model. However, it was difficult to evaluate fiber engagement using this model due to the homogenization of tissue subcomponents. To address this limitation, we developed and validated a multiscale, structure-based FEM to further investigate AF tensile mechanics ("separate model" or SEP) (Zhou et al. 2020). This model was developed based on native human AF, where fibers and extrafibrillar matrix were described as distinct materials occupying separate volumes. This model accurately predicted AF tensile modulus under various loading configurations (e.g. uniaxial tension, biaxial tension, and simple shear) and was able to describe a nonlinear relationship

between specimen geometry and linear-region modulus (Zhou et al. 2020). Moreover, the multiscale model calibration and validation framework allowed us to directly link physical tissue properties with model parameters, broadening its applicability by making parameters modifiable based on structural or compositional changes occurring with degeneration or disease.

Understanding the effect of specimen geometry on fiber-reinforced tissue mechanics is essential for a fundamental understanding of the tissue response under a variety of physiological loads, which benefits the development of tissue repair strategies that aim to recapitulate native tissue behavior. Characterization of the tissue geometry dependence also facilitate the development of experimental designs that capture tissue properties most relevant to the intended applications. Since the separate model is structure-based, AF tensile mechanics can be more comprehensively investigated at both tissue and sub-tissue levels (Zhou et al. 2020). Therefore, the objective of this study was to use the separate model to systematically evaluate the effect of specimen geometry on AF tensile mechanics using a structure-based fiber engagement analysis. While this study was conducted using AF properties, the approach presented here can be easily adapted and applied to other fiber-reinforced biological tissues and engineered composites.

2. Methods

Finite element models were developed to represent rectangular specimens commonly used in uniaxial AF tensile testing (Solidworks 2019; Abaqus 6.14; ANSA 15.2.0; PreView 2.1; FEBio 2.8.5; Mass et al. 2012). Model geometry was created in Solidworks and finite element meshes were generated by ABAQUS and ANSA pre-processor. PreView was used to define the model boundary and loading conditions and the developed model was solved by FEBio. Specimens were oriented along the circumferential-axial direction (**Figure 1A**), consistent with the most commonly tested orientation in the literature for human AF (Acaroglu et al. 1995; Elliott and Setton 2001;

Galante 1967; Guerin and Elliott 2006; Hirsch and Galante 1967; O'Connell et al. 2009; Wagner and Lotz 2004). A structure-based approach was employed to develop the separate model by describing the AF as a fiber-reinforced composite containing distinct materials for the extrafibrillar matrix and fiber bundles ("fibers," **Figure 1A**). All models consisted of three 0.2 mm lamellae with fibers described as full-length cylinders uniformly distributed throughout the lamellae and welded to the surrounding matrix (Goel et al. 1995; Guo et al. 2006; Marchand and Ahmed 1990; Schollum et al. 2010; Shirazi-Adl et al. 1984; Zhou et al. 2020). Fiber bundle diameter was 0.12 mm and interfibrillar spacing was 0.22 mm (Marchand and Ahmed 1990). Fibers were oriented at $\theta = \pm 30^{\circ}$ to represent specimens from the middle-outer region of the anterior AF, the anatomical region most commonly used in experimental tests (**Figure 1B**; Acaroglu et al. 1995; Cassidy et al. 1989; Elliott and Setton 2001; Guerin and Elliott 2006; O'Connell et al. 2009; Wagner and Lotz 2004). To exclude the effect of mesh size on model-predicted mechanics, mesh size was held constant for fiber and matrix elements respectively across all models.

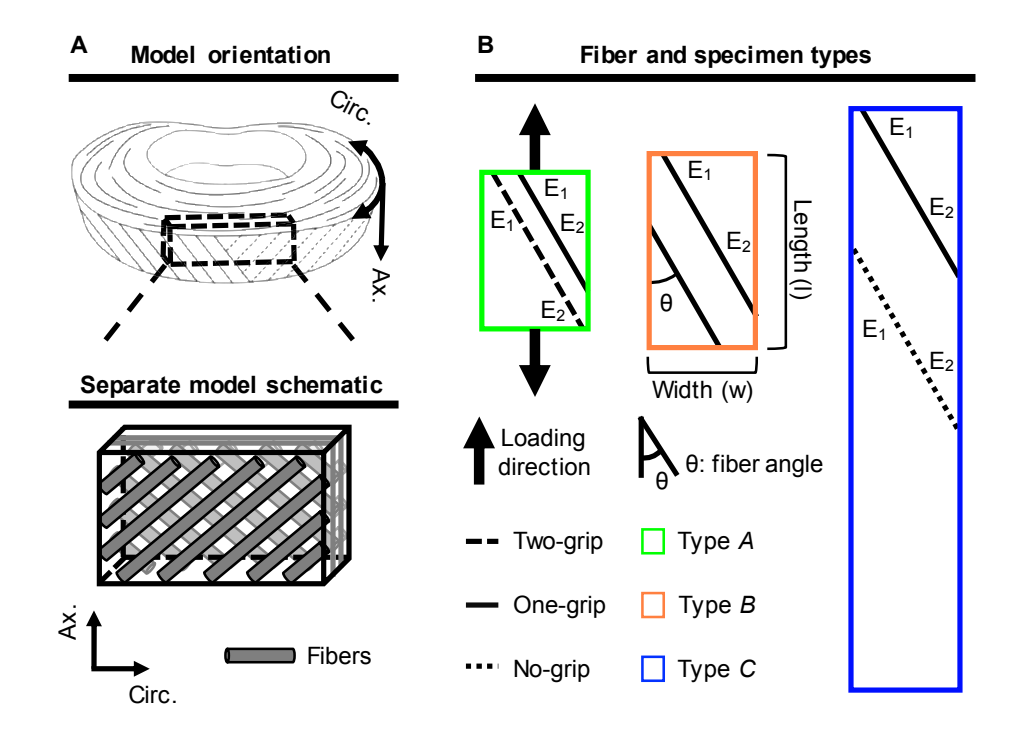


Figure 1: (A) Schematic of model orientation (circumferential: circ.; axial: ax.) and schematic of the separate model, where extrafibrillar matrix and fibers are modeled as distinct materials that occupy separate volumes. (B) Schematic of fiber and specimen types for circumferential-axial specimens. E₁ and E₂ represent the fiber endpoints used in fiber microscopic stress-strain distribution analysis.

Triphasic mixture theory was applied to describe tissue swelling, accounting for specimen hydration (Ateshian et al. 2004; Lai et al. 1991). A Holmes-Mow strain-dependent tissue permeability (k) description was assumed (Equation 1). In Equation 1, I was the determinant of the deformation gradient tensor (F), k_0 represented the hydraulic permeability in the reference configuration ($k_0 = 0.0064 \text{ mm}^4/\text{N·s}$), φ_0 represented the AF solid volume fraction ($\varphi_0 = 0.3$), α represented the power-law exponent ($\alpha = 2$), and M represented the exponential straindependence coefficient (M = 4.8) (Beckstein et al. 2008; Cortes et al. 2014; Gu et al. 1999; Iatridis et al. 1998; Mow et al. 1984; O'Connell et al. 2015). Additionally, model fixed charge density was used to represent tissue proteoglycan content and was set to -100 mmol/L for the matrix obtained from middle-outer AF and 0 mmol/L for the fibers (i.e. no active fiber swelling) (Antoniou et al. 1996; Huyghe et al. 2003; Urban and Maroudas 1979). The osmotic coefficient (0.927) was determined based on a linear interpolation of data reported in Robinson and Stokes (1949) and Partanen et al. (2017). Free diffusivity (D_0) and AF tissue diffusivity (D_{AF}) of Na⁺ and Cl⁻ was set based on data in Gu et al. (2004); 100% ion solubility was assumed ($D_{0,Na^+} = 0.00116 \text{ mm}^2/\text{s}$; $D_{0, Cl^-} = 0.00161 \text{ mm}^2/\text{s}; D_{AF, Na^+} = 0.00044 \text{ mm}^2/\text{s}; D_{AF, Cl^-} = 0.00069 \text{ mm}^2/\text{s}).$

$$k(J) = k_0 \left(\frac{J - \varphi_0}{1 - \varphi_0}\right)^{\alpha} e^{\frac{1}{2}M(J^2 - 1)}$$
 [1]

132

133

134

135

136

137

138

139

140

141

142

143

144

145

146

147

148

149

150

151

153

154

155

156

For the solid content of the AF, the extrafibrillar matrix was modeled as a compressible hyperelastic material using the Neo-Hookean description (**Equation 2**; Guo et al. 2012). I_1 and I_2 were the first and second invariants of the right Cauchy-Green deformation tensor, \boldsymbol{C} ($\boldsymbol{C} = \boldsymbol{F}^T \boldsymbol{F}$), while E_{matrix} and v_{matrix} represented Young's modulus and Poisson's ratio. Fibers were

157 modeled as a compressible hyperelastic ground matrix substance reinforced by power-linear fibers. The ground matrix substance was described using the Holmes-Mow material description. I_1 , I_2 , 158 J, E_{matrix} and ν_{matrix} were defined as described above and eta represented the exponential 159 stiffening coefficient (Equations 3-5) (Holmes and Mow 1990). The power-linear fiber 160 161 description accounted for AF nonlinearity and anisotropy, where γ represented the power-law exponent in the toe-region, E_{lin} represented the fiber modulus in the fiber linear-region, and λ_0 162 163 represented the transition stretch between the toe- and linear-regions (Equation 6). B was a function of γ , $E_{lin.}$, and λ_0 $(B = \frac{E_{lin.}}{2}(\frac{(\lambda_0^2 - 1)}{2(\gamma - 1)} + \lambda_0^2))$. All model parameter values were taken 164 165 from our previous study that calibrated and validated the separate model for tensile mechanics of 166 healthy human AF (Zhou et al. 2020).

167
$$W_{matrix}(I_1, I_2, J) = \frac{E_{matrix}}{4(1 + \nu_{matrix})} (I_1 - 3) - \frac{E_{matrix}}{2(1 + \nu_{matrix})} lnJ + \frac{E_{matrix} \nu_{matrix}}{(1 + \nu_{matrix})(1 - 2\nu_{matrix})} (lnJ)^2$$
 [2]

168
$$W_{fiber}(I_1, I_2, J) = \frac{1}{2}c(e^Q - 1)$$
 [3]

$$Q = \frac{\beta(1 + \nu_{matrix})(1 - 2\nu_{matrix})}{E_{matrix}(1 - \nu_{matrix})} \left[\left(\frac{E_{matrix}}{1 + \nu_{matrix}} - \frac{E_{matrix} \nu_{matrix}}{(1 + \nu_{matrix})(1 - 2\nu_{matrix})} \right) (I_1 - 3) + \frac{E_{matrix} \nu_{matrix}}{(1 + \nu_{matrix})(1 - 2\nu_{matrix})} (I_2 - 2\nu_{matrix}) \right]$$

$$3) - \left(\frac{E_{matrix}}{1 + \nu_{matrix}} + \frac{E_{matrix} \nu_{matrix}}{(1 + \nu_{matrix})(1 - 2\nu_{matrix})}\right) lnJ^{2}]$$
 [4]

$$c = \frac{E_{matrix}(1 - \nu_{matrix})}{2\beta(1 + \nu_{matrix})(1 - 2\nu_{matrix})}$$
 [5]

173

174

175

176

177

172
$$\psi_{n}(\lambda_{n}) = \begin{cases} 0 & \lambda_{n} < 1 \\ \frac{E_{lin.}}{4\gamma(\gamma-1)} (\lambda_{0}^{2} - 1)^{2-\gamma} (\lambda_{n} - 1)^{\gamma} & 1 \leq \lambda_{n} \leq \lambda_{0} \\ E_{lin.}(\lambda_{n} - \lambda_{0}) + B(\lambda_{n}^{2} - \lambda_{0}^{2}) + \frac{E_{lin.}}{4\gamma(\gamma-1)} (\lambda_{0}^{2} - 1)^{2-\gamma} (\lambda_{n} - 1)^{\gamma} & \lambda_{n} > \lambda_{0} \end{cases}$$
 [6]

Sixty multi-lamellar models were created along the circumferential-axial direction ("circumferential specimens," n = 60; **Figure 1A**). To include the range of the specimen geometry reported in the literature for human AF experimental studies, specimen length was varied between 4 and 15 mm in 1 mm increments, and width was varied between 2 and 3 mm in 0.25 mm increments, resulting in length-to-width aspect ratios between 1.33 and 7.50. For each specimen,

fibers were grouped into three categorizations based on their location with respect to the testing grips: "two-grip" fibers (**Figure 1B** – dashed line), "one-grip" fibers (**Figure 1B** – solid line), and "no-grip" fibers (**Figure 1B** – dotted line). Categorizing specimens based on fiber groups resulted in three specimen types: Type A specimens had both two- and one-grip fibers (n = 4, **Figure 1B** – green), Type B specimens had only one-grip fibers (n = 2, **Figure 1B** – orange), and Type C specimens had both one- and no-grip fibers (n = 54, **Figure 1B** – blue); Type C specimens were more representative of typical experimental specimens based on the aspect ratio range (2.0–7.5). To illustrate representative differences between specimen types, one specimen from each type was selected for comparison: specimen representative Type A (w = 2.75 mm, v = 4 mm; Type v = A), specimen representative Type v = A (v = A), and specimen representative Type v = A (v = A), and specimen representative Type v = A (v = A), and specimen representative Type v = A).

Previous studies of AF fiber–matrix interactions suggested that the effective AF matrix stiffness depended on the fiber stretch ratio and hence the applied specimen stretch (Guo et al. 2012). Thus, preliminary work was conducted to assess separate model matrix stress–stretch response to validate the model's capability to investigate fiber–matrix interactions. Validation results showed that despite the pseudo-linear Neo-Hookean matrix material description (**Figure 2A** – dashed line), effective stiffness of the extrafibrillar matrix increased nonlinearly with applied specimen stretch (**Figure 2A** – solid line). Thus, the separate model was considered valid for evaluating fiber–matrix interactions. As such, we added three axial-circumferential models ("axial specimens") in order to explore orientation-dependent differences in fiber–matrix interactions (n = 3). These models were taken from our previous separate model validation study and included only Type *C* specimens with one- and no-grip fibers (**Figure 1B** – $\theta = \pm 60^{\circ}$; Adams and Green 1993; Elliott and Setton 2001; O'Connell et al. 2009). A preliminary study was performed to

evaluate mesh convergence using a randomly selected separate model. Mesh independence was assessed by evaluating the relationship between predicted tissue bulk modulus and mesh size; mesh efficiency was evaluated by assessing the relationship between the model run time and mesh size. The applied mesh for the separate model (**Figure 2B**) was selected to ensure both mesh independence and efficiency (**Figure 2C** – red dashed box).

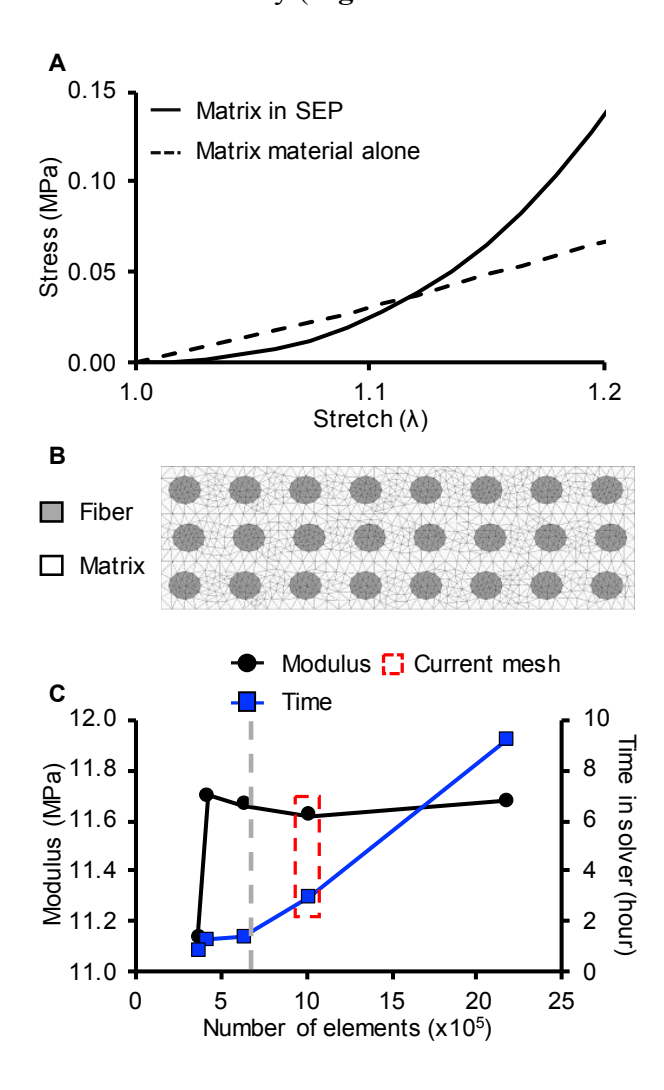


Figure 2: (A) Representative stress—stretch response of the extrafibrillar matrix from the separate model (SEP) demonstrating a nonlinear, stretch-dependent effective matrix stiffness, despite a pseudo-linear matrix material description. (B) Representative finite element mesh shown from the top surface. (C) Results from the mesh convergence study demonstrating mesh independence (based on consistent modulus prediction) and efficiency (based on run time in solver). The gray, vertical dashed line represents the element number threshold, below which the model did not fully converge.

All models were loaded in a two-step process. To account for specimen hydration, free-swelling was simulated in 0.15 M phosphate buffered saline prior to uniaxial tension (Werbner et al. 2019). Then, a uniaxial tensile ramp to 1.2 specimen stretch was applied. During tension, displacement on the top and bottom surfaces was constrained to the loading direction. The post-swelling, pre-tension configuration was defined as the reference configuration. Linear-region modulus was calculated as the slope of the linear-region of the tissue stress–stretch response (1.12–1.15 specimen stretch based on specimen geometry). Bulk AF Poisson's ratio was calculated as the ratio between tissue lateral and longitudinal deformation in the linear-region of the tissue stress-stretch response (1.12–1.15 bulk stretch based on specimen geometry). Fiber reorientation was evaluated as the reorientation magnitude divided by the initial fiber-fiber angle 2θ ("relative fiber reorientation").

Fiber engagement was evaluated at 1.09 specimen stretch for separate models based on the reported transition stretch of type I collagen (Haut 1986; Gentleman et al. 2003; Kato et al. 1989), as well as the reported mean AF fiber bundle transition stretch along the fiber direction (Pham et al. 2018). Engagement was assessed for each fiber element using a stress-based criterion. Fiber elements with stress values below 0.5 MPa, between 0.5 and 24 MPa, and greater than 24 MPa were respectively defined as "not engaged", "engaged", and "damaged." Damaged fiber elements were excluded from all engagement analysis. The engagement threshold (0.5 MPa) was determined based on uniaxial, single lamellar AF tensile tests (Holzapfel et al. 2005). The damage threshold (24 MPa) was determined based on uniaxial type I collagen tensile tests using specimens with similar fiber diameters to the separate model fiber bundles (*i.e.* ~100–200 μm; Haut 1986; Gentleman et al. 2003; Kato et al. 1989; Wang et al. 1994). For each specimen, engagement of a fiber group (*i.e.* two-grip, one-grip, and no-grip fibers) was calculated by dividing the number of

engaged fiber elements of that type by the total number of fiber elements in the specimen; fiber engagement was defined as the sum of the engagement for all fiber groups. Microscopic stress and strain distributions along the fiber length were assessed for all fiber groups (**Figure 1B** – from E₁ to E₂). The relative stress contribution of each tissue subcomponent to the overall stress was determined for both the toe- and linear-regions of the tissue stress–stretch curve (toe-region: 1.03–1.06 stretch based on specimen geometry).

The effect of specimen geometry on AF stress transmission mechanisms was investigated at both the tissue and sub-tissue levels based on stress—strain distributions of specimen front, top, and side surfaces, as well as specimen frontal mid-planes. Finite element models created based on homogenization theory ("homogeneous model") with identical dimensions to specimens a, b, and c described above were developed as a baseline for comparison with the separate models. Similar to separate model parameters, all homogeneous model parameters were taken from our previous separate model calibration and validation study (Zhou et al. 2020). Separate model-predicted mechanical properties were compared to pooled experimental data reported in the literature, where applicable. Pearson correlation strength was determined based on coefficients of correlation ("r"; moderate: -0.7 to -0.5 or 0.5 to 0.7; strong: -1.0 to -0.7 or 0.7 to 1.0). For all statistical analyses, significance was assumed for $p \le 0.05$.

3. Results

In circumferential specimens, less than 1% of fiber elements were considered damaged, while 30–51% of fiber elements were not engaged at 1.09 stretch. Fiber engagement ranged from 49–70% across all circumferential specimens and exhibited a decreasing trend with increasing specimen aspect ratio (**Figure 3A**). Due to the varying engagement of different fiber groups (*i.e.* two-, one-, and no-grip fibers), large differences in model-predicted linear-region modulus were

observed in specimens with comparable geometries and levels of fiber engagement. For example, specimens a, b, and c (Types A, B, and C, respectively) had identical widths, differed by 1 mm of length, and exhibited similar fiber engagement (64–67%; **Figure 3A–B** – representative specimen Type A, B, and C denoted by triangles); however, model-predicted linear-region modulus for representative specimen Type A (31.66 MPa) was 54% greater than that for representative specimen Type B (20.58 MPa) and 92% greater than that for representative specimen Type C (16.47 MPa) due to the 17% two-grip fiber engagement in representative specimen Type D (Figure 3B–D0 – triangles). Model-predicted modulus values were 0.72 \pm 0.06 MPa for axial specimens.

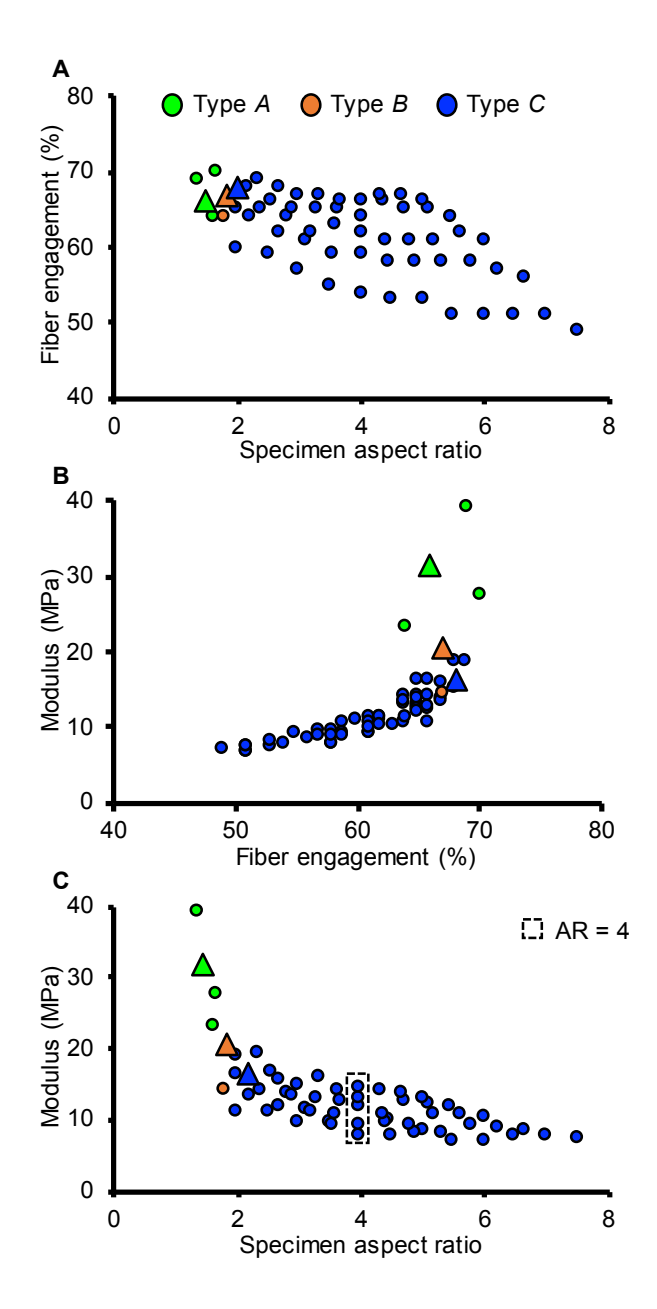


Figure 3: (A) Fiber engagement with respect to specimen aspect ratio for circumferential specimens (n = 60). (B) Separate model-predicted linear-region modulus with respect to fiber engagement for circumferential specimens. (C) Separate model-predicted linear-region modulus with respect to specimen aspect ratio for circumferential specimens. Triangles denote representative specimen Type A, B, and C. Specimens with an aspect ratio (AR) of 4.0 are outlined with a dashed box.

Average fiber stress also depended on specimen type in circumferential specimens. Fibers in Type A specimens experienced the largest stresses. At 1.09 stretch, the average fiber stress in representative specimen Type A (1.87 MPa) was 92% larger than that in representative specimen

Type *B* (1.04 MPa) and 120% larger than that in representative specimen Type *C* (0.85 MPa; **Figure 4A**). However, average fiber strains were comparable between specimen types (**Figure 4B**). Patterns of microscopic stress distribution along the fiber length varied between fiber groups. Although all fiber groups were above the engagement stress threshold (0.5 MPa; **Figure 4C** – gray horizontal dashed line in inset), two-grip fibers exhibited the largest and most uniform stresses along the fiber length (**Figure 4C** – green dashed line). Thus, engagement of two-grip fibers had a greater impact on the predicted linear-region modulus than on fiber engagement. Additionally, microscopic stresses in gripped fibers (*i.e.* two- and one-grip fibers) were largest near the grip-line (E₁) and decreased toward the specimen edge (E₂; **Figure 4C** – dashed and solid lines). Contrary to the microscopic stress distribution along the fiber length, microscopic strain distributions were comparable between fiber groups, with magnitudes ranging between 5 and 35% (**Figure 4D**). In gripped fibers, microscopic strains were smallest at the grip-line (due to the constrained boundaries) and increased toward the specimen edge (**Figure 4D** – solid lines).

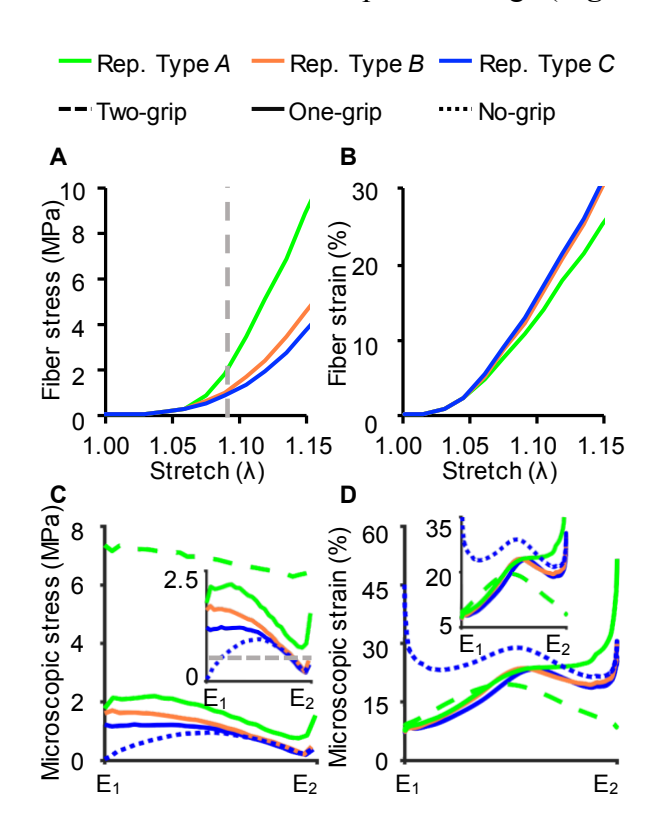


Figure 4: Average fiber (A) stresses and (B) strains with respect to specimen stretch for circumferential representative specimens (rep.) Type A, B, and C. The gray vertical dashed line represents the stretch at which fiber engagement was analyzed ($\lambda = 1.09$). Representative microscopic (C) stress and (D) strain distributions along the fiber length at 1.09 specimen stretch for circumferential specimens. The gray horizontal dashed line highlights the stress threshold for a fiber element to be considered engaged (0.5 MPa). Insets present magnification of subfigures (C) and (D) on a smaller y-axis.

293294

295

296297

298

299

300

301

302

303

304

305

306

307

308

309

310

311

312

313

314

315

316

317

The effect of specimen geometry on fiber engagement was further evaluated for Type C circumferential specimens (n = 54), which were more representative of specimens typically tested in experimental studies. Contributions to engagement from one- and no-grip fibers depended on specimen length: an increase in specimen length resulted in a nonlinear decrease in one-grip fiber engagement (Figure 5A - black circles) and a nonlinear increase in no-grip fiber engagement (Figure 5A – red circles). While one-grip fiber engagement increased with increasing specimen width, a clear relationship could not be observed between no-grip fiber engagement and specimen width. A linear relationship was observed between model-predicted linear-region modulus and each of one- and no-grip fiber engagement. Particularly, a strong positive correlation was observed between one-grip fiber engagement and tissue modulus (Fiber 5B – black line); a moderate negative correlation was observed between no-grip fiber engagement and tissue modulus as tissue tensile modulus decreased with increasing specimen length (Figure 5B – red line). To further evaluate the specimen size effect, five specimens with an aspect ratio of 4.0 were evaluated for linear-region modulus and fiber engagement (**Figure 3C** – dashed box). Between these specimens, it was observed that an increase in specimen size (length or width, Figure 5C only shows the effect of length) resulted in increased one- and no-grip fiber engagement (Figure 5C – red and black circles/lines). It should be noted that the model-predicted linear-region modulus increased with no-grip fiber engagement for specimens with a fixed aspect ratio, which was opposite to the general trend observed for Type C circumferential specimens (Figure 5B versus 5C).

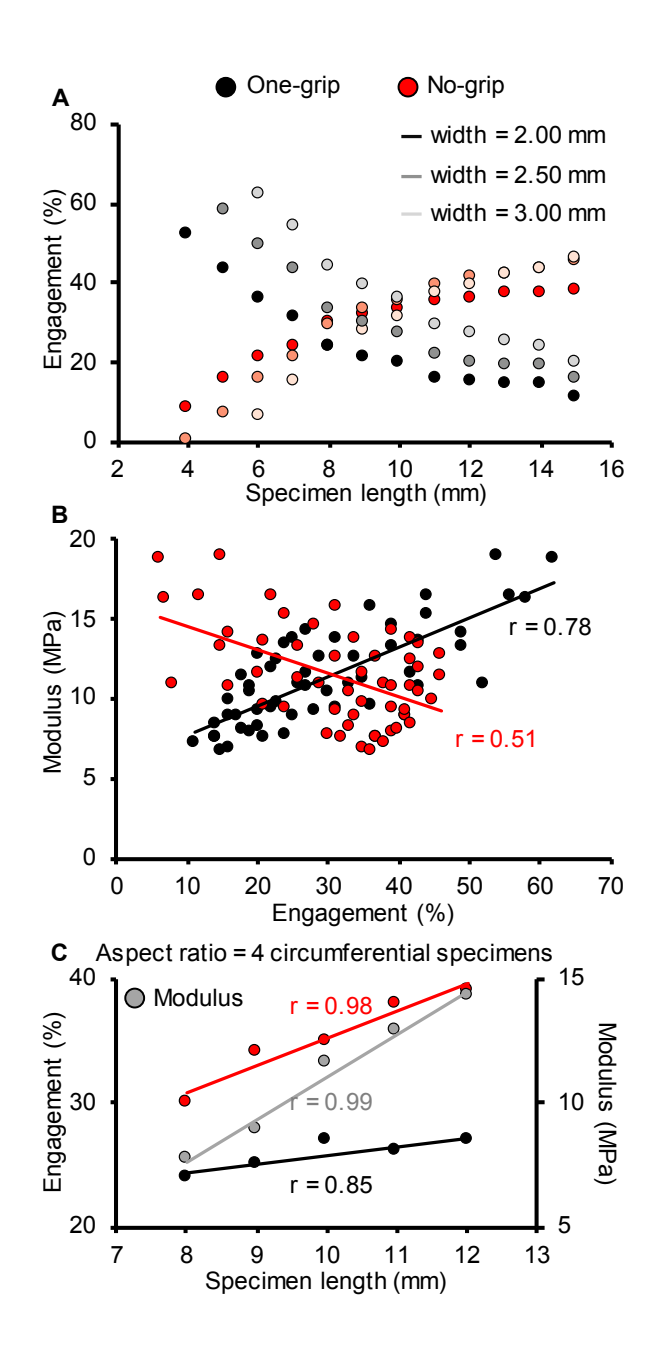


Figure 5: (A) One- and no-grip fiber engagement with respect to specimen length and width for Type C circumferential specimens (n = 54). Specimens with 2.25 mm and 2.75 mm width followed a similar trend but were omitted for clarity. (B) Separate model-predicted linear-region modulus with respect to one- and no-grip fiber engagement for Type C circumferential specimens. (C) One- and no-grip fiber engagement and separate model-predicted linear-region modulus with respect to specimen length for circumferential specimens with an aspect ratio of 4.0 (n = 5).

Applied stress was transmitted from the initially engaged fibers to the surrounding tissue through interfibrillar branches (**Figure 6A** – branches highlighted by white arrows). That is,

stresses were transmitted from gripped fibers, which were loaded immediately after applied tension and thus engaged at a lower specimen stretch, to the remaining tissue through the neighboring matrix and fibers. For Type A specimens, stress was transmitted laterally (*i.e.* transverse to the applied load; **Figure 6A** – Type A, black arrows). For Type C specimens, stress was transmitted longitudinally along the loading direction (**Figure 6A** – Type C, black arrows). Strain concentrations were primarily observed in two-grip fibers near the grip-line in Type A specimens (**Figure 6B** – Type A, red asterisks). However, concentrated strains were observed near the grip-line in one-grip fibers, and in the matrix at the specimen midlength periphery in Type C specimens (**Figure 6B** – Type C, red asterisks). Overall, uniform stress distributions occurred at a lower specimen stretch for Type C specimens than Type C specimens (**Figure 6A**). By contrast, uniform specimen strain distributions occurred earlier in Type C specimens (**Figure 6B**).

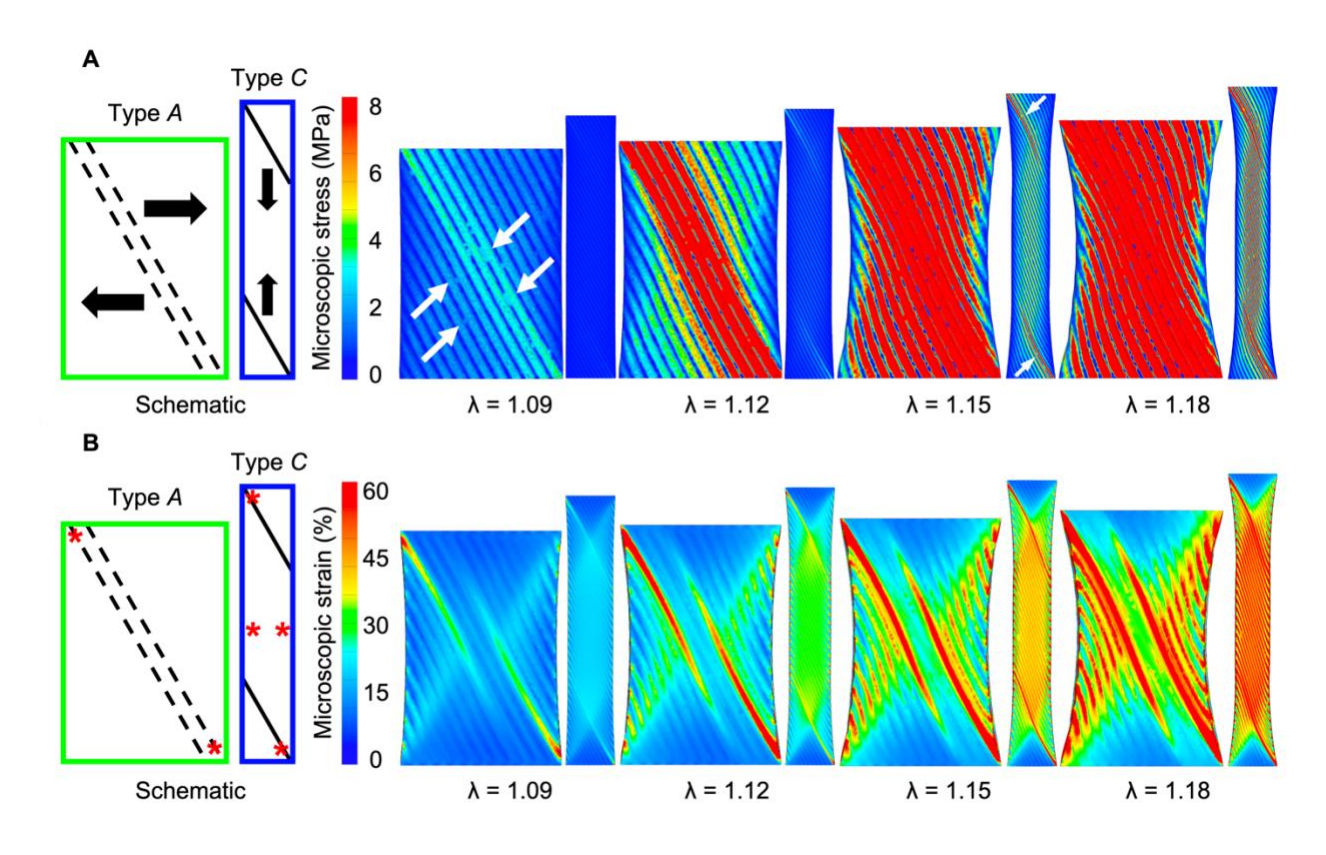


Figure 6: Representative frontal mid-plane (A) stress and (B) strain distributions between 1.09 and 1.18 stretch for Type A and C specimens. The 1.18 stretch step was selected due to

high fiber engagement with minimal concerns for bulk tissue failure, based on experimental results (Acaroglu et al. 1995; Ebara et al. 1996). Black arrows indicate stress transmission directions. White arrows highlight the interfibrillar branches where stresses were transmitted. Red asterisks represent strain concentrations. Specimen Types A and C appear at different scales for clarity. Results for Type B specimens were similar to results for Type A specimens and were omitted for clarity.

Tissue stress distributions differed greatly depending on whether the model was developed based on native tissue architecture (SEP; **Figure 7A**) or homogenization theory (HOM; **Figure 7B**). In SEP models, stresses were dissipated between fibers as described above. By contrast, HOM models exhibited unrealistically large stresses concentrated at grip-lines while providing almost no information regarding stress transmission mechanisms (**Figure 7A** versus **7B** – top surface and frontal mid-plane). At 1.15 specimen stretch, Type *C* specimen stresses were more evenly distributed along the specimen length in SEP models, while stresses were highly concentrated at the grip-line in HOM models (**Figure 7A** versus **7B** – Type *C*). For Type *A* specimens, peak stresses were observed at the grip-line for both SEP and HOM models, but peak HOM stress was 111% larger than peak SEP stress (89.58 versus 42.44 MPa at 1.15 stretch). Contrary to the stress distributions, strain distributions were comparable between SEP and HOM models (**Figure 7C** versus **7D**).

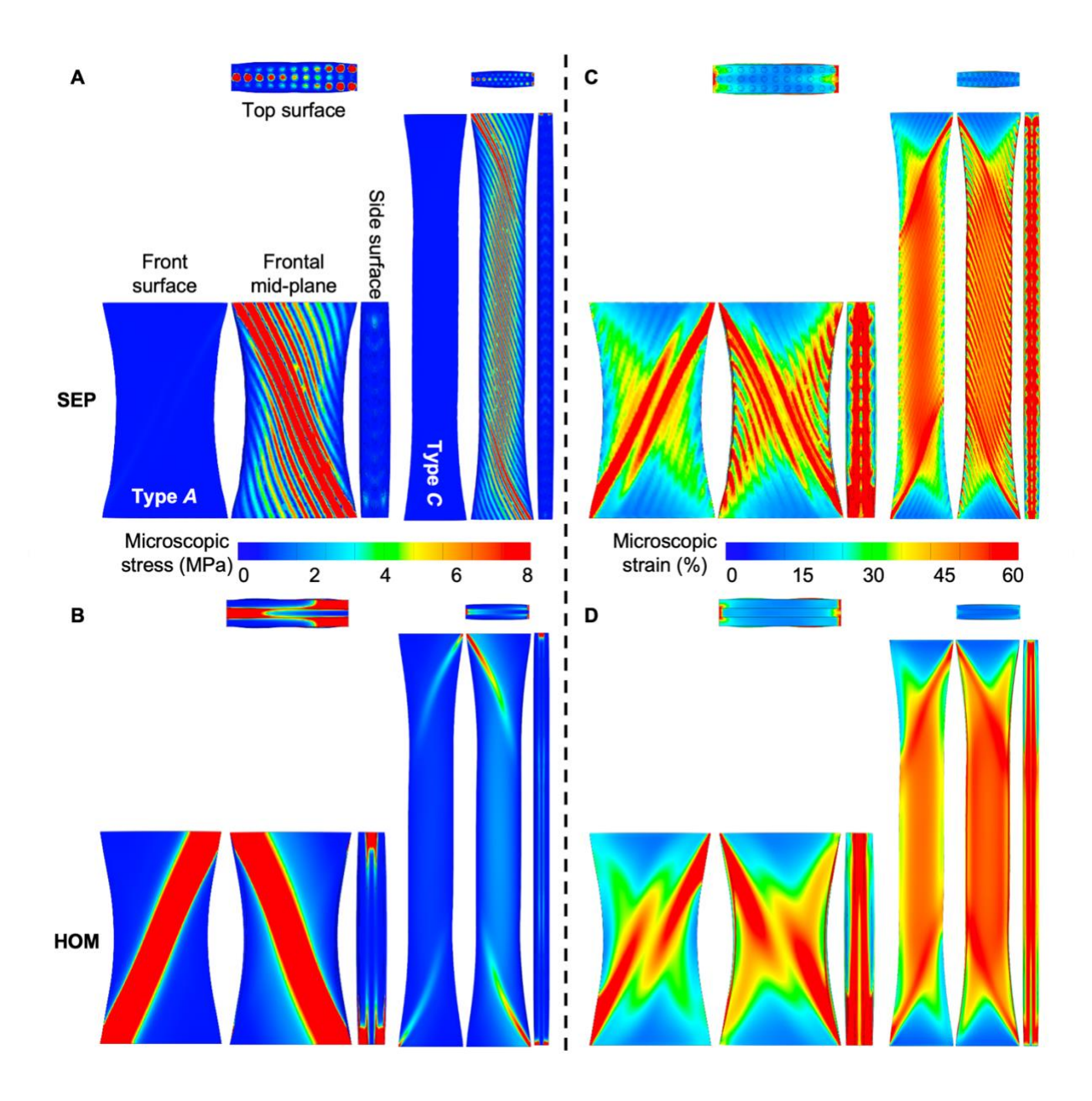


Figure 7: (A) Representative separate model (SEP) stress distributions of front, top, and side surfaces, as well as frontal mid-planes for Types A and C specimens. The same schematic was used in remaining subfigures. (B) Representative homogeneous model (HOM) stress distributions for Types A and C specimens. Representative (C) SEP and (D) HOM strain distributions for Types A and C specimens. All stress and strain distributions were assessed at 1.15 stretch. Specimen Types A and C appear at different scales for clarity. Stress and strain distributions for Type B specimens were similar to those for Type A specimens and were omitted for clarity.

Relative fiber reorientation increased with specimen stretch for all specimens (**Figure 8A**).

Relative fiber reorientation in Type *C* specimens increased linearly with applied stretch, agreeing

with experimental observations (**Figure 8A** – blue circles; Guerin and Elliott 2006; Vergari et al. 2016); Type B specimens followed a similar trend (**Figure 8A** – orange circles). However, Type A specimens exhibited a diminished rate of fiber reorientation after ~1.05 specimen stretch (**Figure 8A** – green circles). In circumferential specimens, relative fiber reorientation was 0.18 ± 0.02 at 1.09 stretch and increased with increasing specimen aspect ratio for Type A and B specimens but exhibited a decreasing trend with aspect ratio for Type C specimens (**Figure 8B**). A similar trend was observed for circumferential Poisson's ratio, where model-predicted Poisson's ratio increased with aspect ratio for Type A and B specimens but exhibited a decreasing trend with aspect ratio for Type C specimens (**Figure 8C**). Model-predicted circumferential Poisson's ratio for Type C specimens was 1.99 ± 0.14 , agreeing with pooled experimental data (**Figure 8C** – inset: p = 0.39; Acaroglu et al. 1995; Elliott and Setton 2001; Guerin and Elliott 2006; O'Connell et al. 2009; Wagner and Lotz 2004). In Type C specimens, a moderate positive correlation was observed between fiber engagement and relative fiber reorientation (**Figure 8D**).

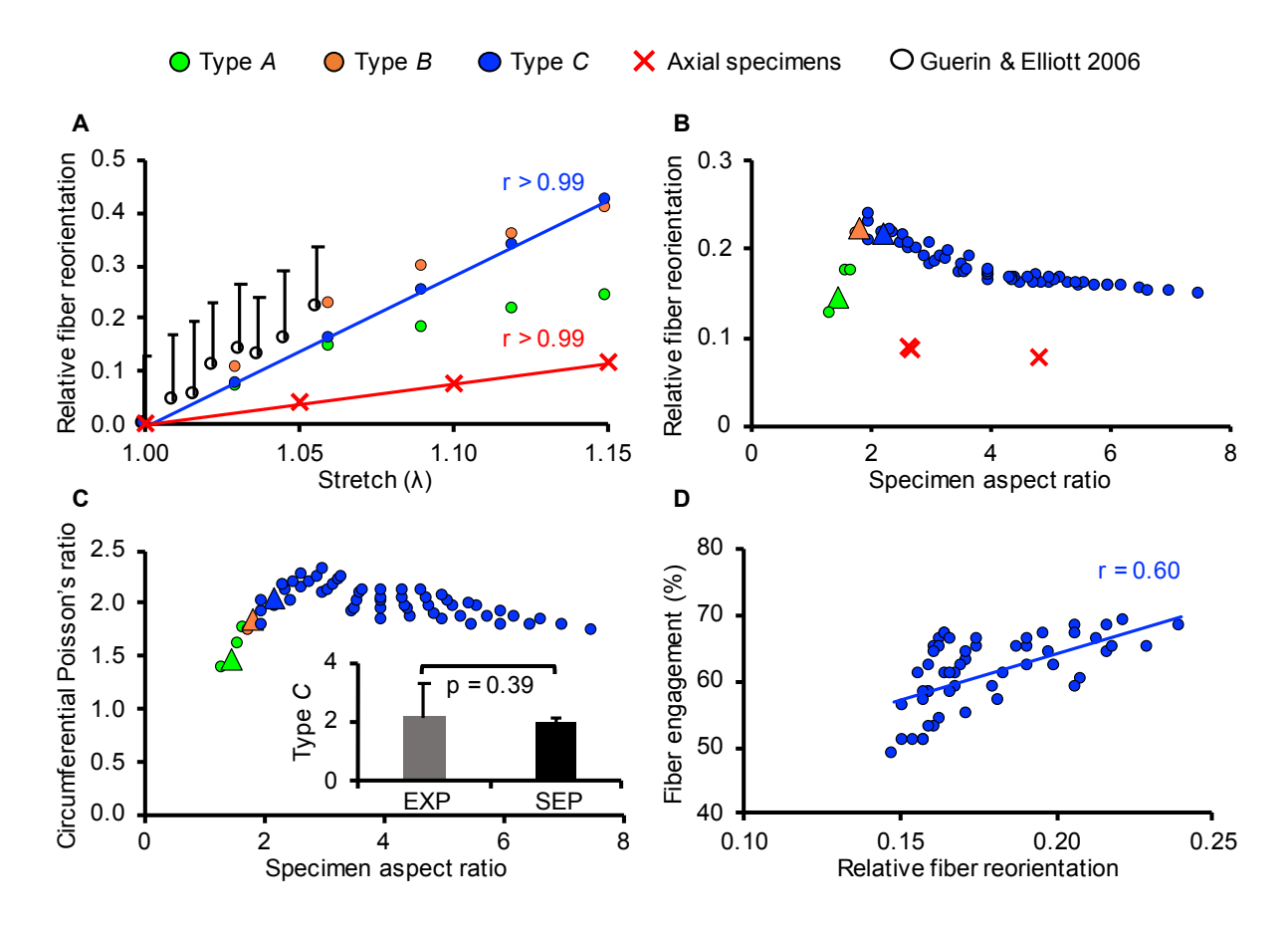


Figure 8: (A) Representative relative fiber reorientation with respect to specimen stretch. Experimental reorientation data in circumferential direction was plotted for comparison (Guerin and Elliott 2006). (B) Relative fiber reorientation with respect to specimen aspect ratio at 1.09 specimen stretch (n = 63). (C) Circumferential Poisson's ratio with respect to specimen aspect ratio (n = 60). Inset: Separate (SEP) model-predicted Poisson's ratio for Type C circumferential specimens compared to pooled experimental (EXP) data. Error bars represent standard deviations. Triangles denote representative specimen Types A, B, and C. (D) Fiber engagement with respect to relative fiber reorientation for Type C circumferential specimens at 1.09 specimen stretch (n = 54).

Axial specimen fiber engagement was < 1% and no fiber elements were considered damaged at 1.09 specimen stretch. In axial specimens, relative fiber reorientation was 0.08 ± 0.01 at 1.09 specimen stretch (**Figure 8B** – red crosses). Fibers were not engaged until ~1.40 specimen stretch, resulting in a pseudo-linear stress–stretch response prior to that point (**Figure 9A** – red line); despite minimal engagement before ~1.40 specimen stretch, fibers immediately began reorienting towards the loading direction. Fiber reorientation in axial specimens occurred at a

lower rate compared to circumferential specimens (**Figure 8A** – red line versus blue line). Model-predicted Poisson's ratio was 0.44 ± 0.10 , which agreed well with pooled experimental data (0.58 \pm 0.25; p = 0.12; Elliott and Setton 2001; O'Connell et al. 2009; Wagner and Lotz 2004).

Fiber and matrix stress–stretch responses in separate models were nonlinear for both circumferential and axial specimens (**Figure 9B**). Fiber and matrix stresses increased less rapidly in axial specimens than in circumferential specimens. In both circumferential and axial specimens, fiber and matrix stress contributions were comparable between the toe- and linear-regions (**Figure 9C**). In circumferential specimens, fibers contributed more than 90% of the total stress while the matrix accounted for the remaining portion. Relative fiber stress contribution in axial specimens was significantly smaller than that in circumferential specimens (p < 0.001). Particularly, fibers contributed ~63% of the total stress while the matrix contributed ~37% (**Figure 9C**).

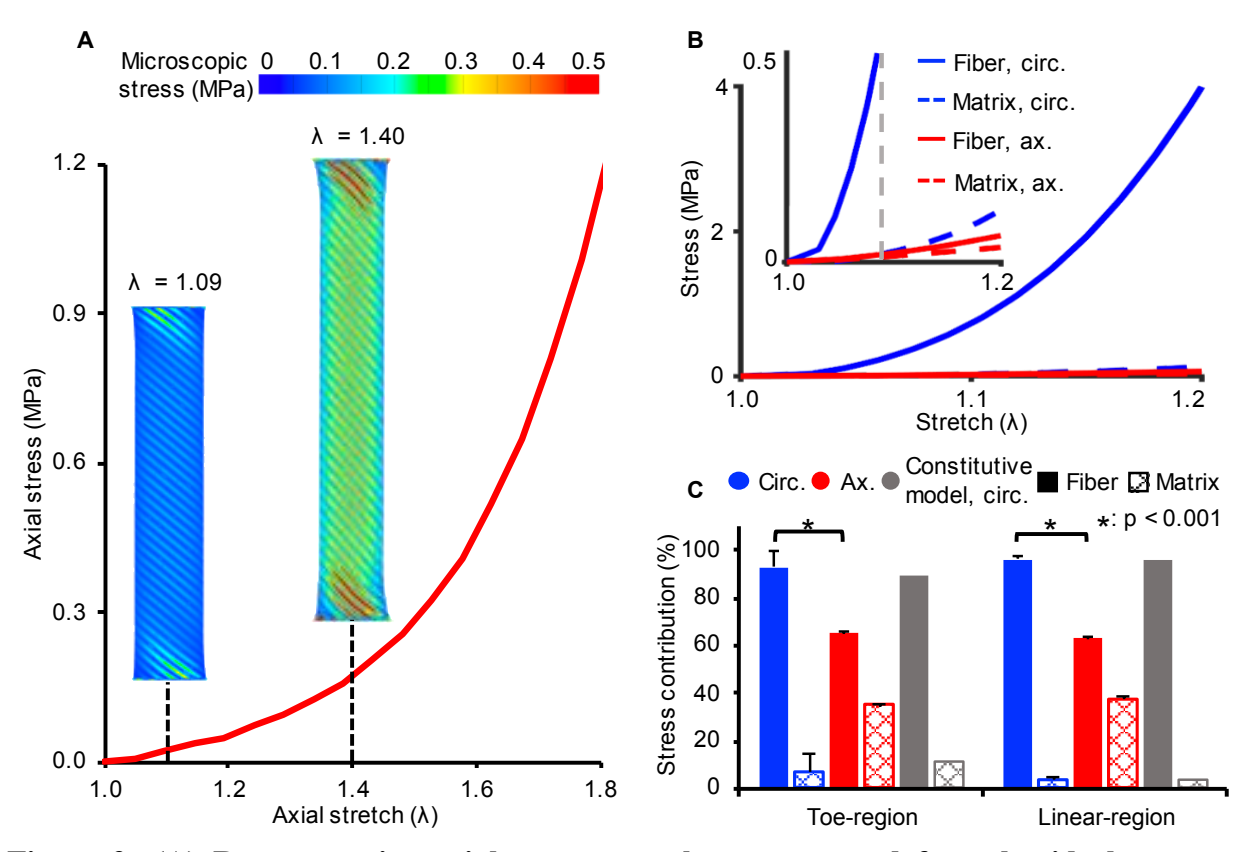


Figure 9: (A) Representative axial stress-stretch response and frontal mid-plane stress distributions at 1.09 and 1.40 specimen stretch. (B) Representative separate model (SEP)

fiber and matrix stress-stretch response in both circumferential (circ.) and axial (ax.) directions. The gray vertical dashed line represents the stretch at which fiber engagement was analyzed ($\lambda=1.09$). (C) Average relative fiber and matrix stress contributions in the toe-and linear-regions for specimens oriented along the circumferential and axial directions. Stress contribution data from a previously published two-dimensional constitutive model is shown for comparison (O'Connell 2009). Error bars represent standard deviations. * denotes p < 0.001.

4. Discussion

This study utilized finite element modeling to investigate the effect of specimen geometry on AF tissue and sub-tissue level tensile mechanics. In particular, our previously validated, multiscale, structure-based FEM was applied to examine the geometry dependence of AF tensile modulus, Poisson's ratio, fiber reorientation behavior, and sub-tissue level stress and strain distributions. The results of this study help explain previously observed variations in AF mechanical properties with respect to specimen geometry and loading orientation. Additionally, these findings reinforce the benefits of explicitly modeling tissue subcomponents when investigating multiscale tissue mechanics, including mechanisms of stress transmission and fiber—matrix interactions.

The modeling framework used in this study facilitated a comprehensive, structure-based fiber engagement analysis. Based on specimen geometry and initial fiber angle, only specimens with small length-to-width aspect ratios contained grip-to-grip fibers that spanned between both grip-lines (*i.e.* aspect ratio < 2.0 for circumferential and < 0.5 for axial specimens). Generally, experimental studies that evaluate AF tensile mechanics along the circumferential direction use specimens with aspect ratios larger than 2.6, which correspond to Type C specimens in our study (Acaroglu et al. 1995; Elliott and Setton 2001; Guerin and Elliott 2006; O'Connell et al. 2009; Wagner and Lotz 2004). Thus, it is expected that none of the circumferential human AF tensile data in the literature accounts for two-grip fiber engagement, which has a larger impact on tissue

tensile mechanics than one- and no-grip fibers due to additional boundary constraints that significantly increase fiber stresses (**Figure 4C**). The significant contribution of two-grip fibers has been experimentally corroborated in the axial direction, as previous studies showed that axial modulus differed by an order of magnitude due to the engagement of two-grip fibers in wide specimens tested with adjacent vertebrae (Adams and Green 1993; Green et al. 1993; Elliott and Setton 2001; O'Connell et al. 2009).

The results of this study help explain the disproportionate increase in AF axial tensile modulus with specimen width that was previously reported in the literature (Adams and Green 1993). Work by Adams and Green (1993) developed a mathematical fiber engagement model that suggested a linear relationship between axial tensile modulus and effective fiber length (*i.e.* fiber engagement) to account for variations in AF axial tensile modulus with specimen width. However, fiber engagement only partially accounted for variations in bulk tensile modulus. For example, representative specimen Type A and C had almost identical fiber engagement (66% versus 68%), but representative specimen Type A contained two-grip fibers and had a predicted linear-region modulus that was ~92% greater than that of representative specimen Type C (31.66 versus 16.47 MPa, **Figure 3**), which had no two-grip fibers. The mathematical fiber engagement model developed by Adams and Green would fail to sufficiently predict this modulus difference (mathematical model predicted difference: 12%) since it was not able to differentiate the engagement of different fiber groups.

Varying engagement of distinct fiber groups may also help explain the large differences between the tensile mechanics of tissues with aligned fibers and off-axis, angle-ply fibers (**Figure** $1B - \theta \neq \pm 0^{\circ}$ or 90°). For example, the mean reported human Achilles tendon tensile modulus ranged from 262 to 819 MPa (DeFrate et al. 2006; Hansen et al. 2012; Louis-Ugbo et al. 2004;

Shaw and Lewis 1997; Wren et al. 2001), which was an order of magnitude larger than the mean reported human AF circumferential linear-region modulus, which ranged from 18 to 29 MPa (Acaroglu et al. 1995; Elliott and Setton 2001; Guerin and Elliott 2006; O'Connell et al. 2009). Since the higher glycosaminoglycan content in the AF is not considered a major contributor to tensile mechanics along the fiber direction (Screen et al. 2006; Szczesny and Elliott 2014; Szczesny et al. 2017), differences in reported moduli may be largely due to differences in patterns of fiber engagement based on mechanical test specimen boundary conditions. That is, tendons have aligned collagen fibers that span between both testing grips while most AF specimens have no two-grip fibers. The lack of two-grip fiber engagement during testing can result in an underestimation of AF tensile properties, which are crucial for developing tissue repair and replacement strategies (Long et al. 2016; O'Connell et al. 2015).

Explicitly modeling tissue subcomponents proved essential for examining stress transmission mechanisms, which are difficult to quantify experimentally in specimens containing off-axis fibers. The separate model predicted that stress was transmitted through interfibrillar branches (**Figure 6A** – white arrows), agreeing with experimental observations in tendons and highlighting the importance of fiber–matrix interactions (Szczesny and Elliott 2014; Szczesny et al. 2017). The separate model also elucidated an important energy dissipation mechanism via redistribution of stresses throughout the tissue with increasing specimen stretch (**Figure 6A** and **7A** – SEP), which was consistent with previous observations obtained from tendon shear lag models (Szczesny and Elliott 2014). Employing homogenization theory for model development provided more computationally efficient models, however these models were not capable of replicating tissue stress transmission and energy dissipation behaviors and resulted in large and physiologically improbable stresses (**Figure 6A** and **7B** – HOM).

Fiber–matrix interactions help explain disparities between experimental measurements and computational model input parameters. Experimental measurements of AF tissue-level Poisson's ratio, especially in the circumferential direction, are often more than three times larger than the theoretical limit for incompressible materials (theoretical maximum = 0.5) (**Table 1**; Acaroglu et al. 1995; Elliott and Setton 2001; Guerin and Elliott 2006; O'Connell et al. 2009; Wagner and Lotz 2004). The matrix substance in the separate model was defined with a Poisson's ratio of 0.3. Results from this study showed that fiber engagement increased with fiber reorientation, which led to greater tissue contraction in the transverse direction and hence larger bulk circumferential Poisson's ratio values compared to the pre-defined matrix Poisson's ratio (1.99 versus 0.3).

Table 1: Summary of anterior annulus fibrosus in-plane Poisson's ratio data reported in the literature (circ.: circumferential; ax.: axial). Data were pooled when applicable. Poisson's ratio values were reported as "mean (standard deviation)." Experimental data taken from Acaroglu et al. 1995, Elliott and Setton 2001, Guerin and Elliott 2006, O'Connell et al. 2009, and Wagner and Lotz 2004.

	Anterior outer annulus fibrosus								Anterior inner annulus fibrosus		
	Circax.					Axcirc.			Circax.		Axcirc.
	Acaroglu et al. 1995	Elliott& Setton 2001	Wagner& Lotz 2004	Guerin& Elliott 2006	O'Connell et al. 2009	Elliott& Setton 2001	Wagner& Lotz 2004	O'Connell et al. 2009	Acaroglu et al. 1995	Elliott& Setton 2001	Elliott& Setton 2001
n	15	20	5	8	7	9	5	7	15	8	7
Poisson's ratio	1.16 (0.68)	1.77 (0.65)	2.32 (0.87)	4.64 (4.12)	2.27 (0.87)	0.66 (0.22)	0.40 (0.15)	0.61 (0.35)	1.48 (0.66)	1.86 (2.06)	1.58 (0.67)
Pooled value	2.13 (1.19)			0.58 (0.25)			1.61 (1.13)		1.58 (0.67)		

Fiber-matrix interactions also partially account for AF anisotropy. In the current study, axial specimens had significantly less fiber engagement compared to circumferential specimens (49–70%) due to significantly smaller fiber reorientation (77% difference, p < 0.001). The lower axial fiber engagement significantly decreased the relative fiber stress contribution, resulting in lower tensile moduli and Poisson's ratios. The separate model predicted a tensile modulus of 11.36 \pm 3.00 MPa and Poisson's ratio of 1.99 \pm 0.14 for circumferential specimens; these values are 4–10 times larger than those for axial specimens (0.72 \pm 0.06 MPa and 0.44 \pm 0.11, respectively). Additionally, fiber-matrix interactions played an important role in specimen size effects. The 85%

increase in modulus across the range of specimen lengths was attributable to a 30% increase in nogrip fiber engagement, which arose from increased fiber-matrix interactions in larger specimens (**Figure 5C**).

511

512

513

514

515

516

517

518

519

520

521

522

523

524

525

526

527

528

529

530

531

532

Knowledge of sub-tissue level mechanical response is important for experimental designs (Avazmohammadi et al. 2018). Limited tissue availability often determines specimen aspect ratio. For example, reported AF circumferential specimen aspect ratios vary between 2.6 and 5.6 (i.e. Type C specimens in this study; Acaroglu et al. 1995; Elliott and Setton 2001; Guerin and Elliott 2006; O'Connell et al. 2009). Our results, together with previous data, suggest that specimens with larger aspect ratios (aspect ratio > 4) have smaller variations in modulus and an increased likelihood of midlength failure based on local strain-based failure criteria (Werbner et al. 2017). However, due to limited stress transmission in these specimens, mechanical properties may be underestimated for applications that require a high level of fiber engagement, such as multilaminate angle-ply collagen patches (McGuire et al. 2017). Reducing specimen aspect ratio (aspect ratio < 4) resulted in larger and more uniform patterns of fiber engagement, and the boundary conditions better mimicked the *in vivo* anatomical constraints (White and Panjabi 1990). However, the use of such specimens is often avoided experimentally due to a higher likelihood of grip-line failure during testing (Werbner et al. 2017). These findings highlight the importance of reporting the tested specimen geometry in order to properly compare measured mechanical properties across studies. Additionally, the approach used in this study has the potential to guide the optimization of future experimental designs under the constraints imposed by tissue availability: researchers can perform parametric finite element modeling studies and adjust testing or data analysis protocols for the intended applications in order to obtain more relevant tissue mechanical properties.

Alternatively, planar biaxial loading can be used to increase fiber engagement during mechanical testing. Constraining or loading specimens in the transverse direction will make all fibers extend between testing grips (*i.e.* two-grip fibers), resulting in increased fiber engagement. Additionally, previous work showed that constitutive models developed using planar biaxial datasets more accurately predicted tissue mechanics under alternate loading modalities compared to models developed using only uniaxial tensile datasets (O'Connell et al. 2012). Unfortunately, limited tissue availability and complex testing setups have limited the use of biaxial biological tissue testing (Sun et al. 2005). Our previous work showed that the separate model can accurately describe AF mechanics under planar biaxial tension (Zhou et al. 2020). Thus, using uniaxial test data as a calibration input, the separate model can further complement experimental studies with more comprehensive investigations of complex loading conditions that better mimic physiological loading conditions.

One limitation to this study was that the natural anatomical curvature of the disc was neglected when creating tissue-level rectangular specimen geometries, which could be an additional factor contributing to geometry-dependent tissue mechanics. Secondly, tissue damage was assessed using a local stress-based criterion; however, previous studies have suggested that AF failure may be driven by local strains (Werbner et al. 2017) or strain energy density (Ayturk et al. 2010; Ayturk et al. 2012). While the focus of this work was on fiber engagement, future work will investigate damage accumulation at the sub-tissue level. Additionally, the current model used a simplified fiber network and did not include descriptions of fiber dispersion or variations in fiber density and diameter, which have been shown to be associated with degeneration and diseases such as diabetes (Adams and Roughley 2006; Guo et al. 2012; Li et al. 2013; Svensson et al. 2018).

Therefore, subsequent model iterations will include variations in tissue structure (*e.g.* fiber diameter and density) and composition (*e.g.* proteoglycan content).

This study used a multiscale, structure-based finite element model to examine the multiscale mechanics of annulus fibrosus specimens under uniaxial tensile loading. The model accurately predicted variations in tissue level tensile mechanics such as modulus and Poisson's ratio, as well as sub-tissue level mechanics such as fibrillar stress distributions and fiber reorientation. Additionally, the results of this study elucidated important tissue stress transmission mechanisms, relative tissue subcomponent stress contributions, and fiber—matrix interactions. This study also provided a potential combined computational-experimental design framework for fiber-reinforced biological tissues. In conclusion, the methods presented here can be used in conjunction with experimental data to simultaneously investigate both tissue and sub-tissue scale mechanics, which is important as the field of soft tissue biomechanics advances towards studies that focus on tissue degeneration, disease, and injury at smaller length scales (Iatridis and Gwynn 2004; Vergari et al. 2016).

571	Acknowledgements

The work was supported by the National Science Foundation (CMMI: 1760467).

573 **Conflict of Interest**

574 The authors declare no conflict of interest.

Reference

- Acaroglu ER, Iatridis JC, Setton LA, Foster RJ, Mow VC, Weidenbaum M (1995). Degeneration
- and aging affect the tensile behavior of human lumbar anulus fibrosus. Spine, 20(24), 2690-
- 578 2701. https://doi.org/10.1097/00007632-199512150-00010

Adams MA, Green TP (1993). Tensile properties of the annulus fibrosus. European Spine Journal, 2(4), 203-208. https://doi.org/10.1007/BF00299447

Adams MA, Roughley PJ (2006). What is intervertebral disc degeneration, and what causes it?. Spine, 31(18), 2151-2161. https://doi.org/10.1097/01.brs.0000231761.73859.2c

Antoniou J, Steffen T, Nelson F, Winterbottom N, Hollander AP, Poole RA, Aebi M, Alini M (1996). The human lumbar intervertebral disc: evidence for changes in the biosynthesis and denaturation of the extracellular matrix with growth, maturation, ageing, and degeneration. The Journal of clinical investigation, 98(4), 996-1003. https://doi.org/10.1172/JCI118884

Ateshian GA, Chahine NO, Basalo IM, Hung CT (2004). The correspondence between equilibrium biphasic and triphasic material properties in mixture models of articular cartilage. Journal of biomechanics, 37(3), 391-400. https://doi.org/10.1016/S0021-9290(03)00252-5

Avazmohammadi R, Li DS, Leahy T, Shih E, Soares JS, Gorman JH, Gorman RC and Sacks MS (2018). An integrated inverse model-experimental approach to determine soft tissue three-dimensional constitutive parameters: Application to post-infarcted myocardium. Biomechanics and modeling in mechanobiology, 17(1), 31-53. https://doi.org/10.1007/s10237-017-0943-1

Ayturk UM, Garcia JJ and Puttlitz CM (2010). The micromechanical role of the annulus fibrosus components under physiological loading of the lumbar spine. Journal of biomechanical engineering, 132(6). https://doi.org/10.1115/1.4001032

Ayturk UM, Gadomski B, Schuldt D, Patel V and Puttlitz CM (2012). Modeling degenerative disk disease in the lumbar spine: a combined experimental, constitutive, and computational approach. Journal of biomechanical engineering, 134(10). https://doi.org/10.1115/1.4007632

Bass EC, Ashford FA, Segal MR, Lotz JC (2004). Biaxial testing of human annulus fibrosus and its implications for a constitutive formulation. Annals of biomedical engineering, 32(9), 1231-1242. https://doi.org/10.1114/B:ABME.0000039357.70905.94

Beckstein JC, Sen S, Schaer TP, Vresilovic EJ, Elliott DM (2008). Comparison of animal discs used in disc research to human lumbar disc: axial compression mechanics and glycosaminoglycan content. Spine, 33(6), E166-E173. https://doi.org/10.1097/BRS.0b013e318166e001

- Cassidy JJ, Hiltner A, Baer E (1989). Hierarchical structure of the intervertebral disc. Connective
- 619 tissue research, 23(1), 75-88. https://doi.org/10.3109/03008208909103905

- 620 Cortes DH, Jacobs NT, DeLucca JF, Elliott DM (2014). Elastic, permeability and swelling
- properties of human intervertebral disc tissues: A benchmark for tissue engineering. Journal of
- 622 biomechanics, 47(9), 2088-2094. https://doi.org/10.1016/j.jbiomech.2013.12.021

- DeFrate LE, van der Ven A, Boyer PJ, Gill TJ and Li G (2006). The measurement of the
- variation in the surface strains of Achilles tendon grafts using imaging techniques. Journal of
- 626 biomechanics, 39(3), 399-405. https://doi.org/10.1016/j.jbiomech.2004.12.021

627

- Ebara S, Iatridis JC, Setton LA, Foster RJ, Mow VC and Weidenbaum M (1996). Tensile properties of nondegenerate human lumbar anulus fibrosus. Spine, 21(4), 452-461.
- 630 https://doi.org/10.1097/00007632-199602150-00009

631

- Eberlein R, Holzapfel GA, Schulze-Bauer CAJ (2001). An anisotropic model for annulus tissue
- and enhanced finite element analyses of intact lumbar disc bodies. Computer methods in
- biomechanics and biomedical engineering, 4(3), 209-229.
- https://doi.org/10.1080/10255840108908005

636

- Elliott DM, Setton LA (2001). Anisotropic and inhomogeneous tensile behavior of the human
- anulus fibrosus: experimental measurement and material model predictions. Journal of
- 639 biomechanical engineering, 123(3), 256-263. https://doi.org/10.1115/1.1374202

640

- Eskandari M, Nordgren TM, O'Connell GD (2019). Mechanics of pulmonary airways: Linking
- structure to function through constitutive modeling, biochemistry, and histology. Acta
- biomaterialia. https://doi.org/10.1016/j.actbio.2019.07.020

644

- Galante J (1967). Tensile properties of the human lumbar annulus fibrosus. Acta Orthopaedica
- 646 Scandinavica, 38(sup100), 1-91. https://doi.org/10.3109/ort.1967.38.suppl-100.01

647

- 648 Gentleman E, Lay AN, Dickerson DA, Nauman EA, Livesay GA and Dee KC (2003).
- Mechanical characterization of collagen fibers and scaffolds for tissue engineering. Biomaterials.
- 650 24(21), 3805-3813. https://doi.org/10.1016/S0142-9612(03)00206-0

651

- 652 Goel VK, Monroe BT, Gilbertson LG, Brinckmann P (1995). Interlaminar shear stresses and
- laminae separation in a disc: finite element analysis of the L3-L4 motion segment subjected to
- axial compressive loads. Spine, 20(6), 689-698. https://doi.org/10.1097/00007632-199503150-
- 655 00010

656

- 657 Green TP, Adams MA, Dolan P (1993). Tensile properties of the annulus fibrosus. European
- 658 Spine Journal, 2(4), 209-214. https://doi.org/10.1007/BF00299448

659

- 660 Gu WY, Mao XG, Foster RJ, Weidenbaum M, Mow VC, Rawlins BA (1999). The anisotropic
- hydraulic permeability of human lumbar anulus fibrosus: influence of age, degeneration,
- direction, and water content. Spine, 24(23), 2449. https://doi.org/10.1097/00007632-199912010-
- 663 00005

- 665 Gu WY, Yao H, Vega AL, Flagler D (2004). Diffusivity of ions in agarose gels and
- intervertebral disc: effect of porosity. Annals of biomedical engineering, 32(12), 1710-1717.
- https://doi.org/10.1007/s10439-004-7823-4

- Guerin HL, Elliott DM (2006). Degeneration affects the fiber reorientation of human annulus fibrosus under tensile load. Journal of biomechanics, 39(8), 1410-1418.
- https://doi.org/10.1016/j.jbiomech.2005.04.007

672

673 Guerin HL, Elliott DM (2007). Quantifying the contributions of structure to annulus fibrosus 674 mechanical function using a nonlinear, anisotropic, hyperelastic model. Journal of Orthopaedic 675 Research, 25(4), 508-516. https://doi.org/10.1002/jor.20324

676

Guo ZY, Peng XQ and Moran B (2006). A composites-based hyperelastic constitutive model for soft tissue with application to the human annulus fibrosus. Journal of the Mechanics and Physics of Solids, 54(9), 1952-1971. https://doi.org/10.1016/j.jmps.2006.02.006

680

- 681 Guo Z, Shi X, Peng X, Caner F (2012). Fibre–matrix interaction in the human annulus fibrosus. Journal of the mechanical behavior of biomedical materials, 5(1), 193-205.
- 683 https://doi.org/10.1016/j.jmbbm.2011.05.041

684

- Hansen P, Kovanen V, Hölmich P, Krogsgaard M, Hansson P, Dahl M, Hald M, Aagaard P,
- Kjaer M and Magnusson SP (2013). Micromechanical properties and collagen composition of
- ruptured human achilles tendon. The American journal of sports medicine, 41(2), 437-443.
- 688 https://doi.org/10.1177/0363546512470617

689

- Hirsch C and Galante J (1967). Laboratory conditions for tensile tests in annulus fibrosus from human intervertebral discs. Acta Orthopaedica Scandinavica, 38(1-4), 148-162.
- 692 https://doi.org/10.3109/17453676708989629

693

- Holmes MH, Mow VC (1990). The nonlinear characteristics of soft gels and hydrated connective tissues in ultrafiltration. Journal of biomechanics, 23(11), 1145-1156.
- 696 https://doi.org/10.1016/0021-9290(90)90007-P

697 698

Holzapfel GA, Schulze-Bauer CAJ, Feigl G, Regitnig P (2005). Single lamellar mechanics of the human lumbar anulus fibrosus. Biomechanics and modeling in mechanobiology, 3(3), 125-140. https://doi.org/10.1007/s10237-004-0053-8

700 701 702

699

Huyghe JM, Houben GB, Drost MR, Van Donkelaar CC (2003). An ionised/non-ionised dual porosity model of intervertebral disc tissue. Biomechanics and modeling in mechanobiology, 2(1), 3-19. https://doi.org/10.1007/s10237-002-0023-y

704 705 706

703

Iatridis JC, Setton LA, Foster RJ, Rawlins BA, Weidenbaum M, Mow VC (1998). Degeneration affects the anisotropic and nonlinear behaviors of human anulus fibrosus in compression. Journal of biomechanics, 31(6), 535-544. https://doi.org//10.1016/S0021-9290(98)00046-3

708 709

- 710 Iatridis JC, ap Gwynn I (2004). Mechanisms for mechanical damage in the intervertebral disc
- annulus fibrosus. Journal of biomechanics, 37(8), 1165-1175.
- 712 https://doi.org/10.1016/j.jbiomech.2003.12.026

- 714 Kato YP, Christiansen DL, Hahn RA, Shieh SJ, Goldstein JD and Silver FH (1989). Mechanical
- properties of collagen fibres: a comparison of reconstituted and rat tail tendon fibres.
- 716 Biomaterials, 10(1), 38-42. https://doi.org/10.1016/0142-9612(89)90007-0

717

- 718 Klisch SM, Lotz JC (1999). Application of a fiber-reinforced continuum theory to multiple
- deformations of the annulus fibrosus. Journal of biomechanics, 32(10), 1027-1036.
- 720 https://doi.org/10.1016/S0021-9290(99)00108-6

721

- Lai WM, Hou JS, Mow VC (1991). A triphasic theory for the swelling and deformation
- behaviors of articular cartilage. Journal of biomechanical engineering, 113(3), 245-258.
- 724 https://doi.org/10.1115/1.2894880

725

- Lechner K, Hull ML and Howell SM (2000). Is the circumferential tensile modulus within a
- human medial meniscus affected by the test sample location and cross-sectional area?. *Journal of*
- 728 orthopaedic research, 18(6), 945-951. https://doi.org/10.1002/jor.1100180614

729

- 730 Li Y, Fessel G, Georgiadis M, Snedeker JG (2013). Advanced glycation end-products diminish
- tendon collagen fiber sliding. Matrix biology, 32(3-4), 169-177.
- 732 https://doi.org/10.1016/j.matbio.2013.01.003

733

- Long RG, Torre OM, Hom WW, Assael DJ and Iatridis JC (2016). Design requirements for
- annulus fibrosus repair: review of forces, displacements, and material properties of the
- intervertebral disk and a summary of candidate hydrogels for repair. Journal of biomechanical
- 737 engineering, 138(2). https://doi.org/10.1115/1.4032353

738

- 739 Louis-Ugbo J, Leeson B and Hutton WC (2004). Tensile properties of fresh human calcaneal
- 740 (Achilles) tendons. Clinical Anatomy: The Official Journal of the American Association of
- 741 Clinical Anatomists and the British Association of Clinical Anatomists, 17(1), 30-35.
- 742 https://doi.org/10.1002/ca.10126

743

- Marchand FR, Ahmed AM (1990). Investigation of the laminate structure of lumbar disc anulus
- 745 fibrosus. Spine, 15(5), 402-410. https://doi.org/10.1097/00007632-199005000-00011

746

- Maas SA, Ellis BJ, Ateshian GA, Weiss JA (2012). FEBio: finite elements for
- biomechanics. Journal of biomechanical engineering, 134(1), 011005.
- 749 <u>https://doi.org/10.1115/1.4005694</u>

750

- 751 McGuire R, Borem R and Mercuri J (2017). The fabrication and characterization of a multi-
- laminate, angle-ply collagen patch for annulus fibrosus repair. Journal of tissue engineering and
- regenerative medicine, 11(12), 3488-3493. https://doi.org/10.1002/term.2250

- 755 Mow VC, Holmes MH, Lai WM (1984). Fluid transport and mechanical properties of articular
- 756 cartilage: a review. Journal of biomechanics, 17(5), 377-394. https://doi.org/10.1016/0021-
- 757 9290(84)90031-9

759 O'Connell GD (2009). Degeneration Affects the Structural and Tissue Mechanics of the 760 Intervertebral Disc. Publicly Accessible Penn Dissertations. 85.

761

762 O'Connell GD, Guerin HL, Elliott, DM (2009). Theoretical and uniaxial experimental evaluation 763 of human annulus fibrosus degeneration. Journal of biomechanical engineering, 131(11), 764 111007. https://doi.org/10.1115/1.3212104

765

766 O'Connell GD, Sen S, Elliott DM (2012). Human annulus fibrosus material properties from 767 biaxial testing and constitutive modeling are altered with degeneration. Biomechanics and 768 modeling in mechanobiology, 11(3-4), 493-503. https://doi.org/10.1007/s10237-011-0328-9

769 770

O'Connell, GD, Leach JK, Klineberg EO (2015). Tissue engineering a biological repair strategy for lumbar disc herniation. BioResearch open access, 4(1), 431-445. https://doi.org/10.1089/biores.2015.0034

772 773 774

775

776

771

Partanen JI, Partanen LJ, Vahteristo KP (2017). Traceable thermodynamic quantities for dilute aqueous sodium chloride solutions at temperatures from (0 to 80) C. Part 1. Activity coefficient, osmotic coefficient, and the quantities associated with the partial molar enthalpy. Journal of Chemical & Engineering Data, 62(9), 2617-2632. https://doi.org/10.1021/acs.jced.7b00091

777 778 779

Pham DT, Shapter JG and Costi JJ (2018). Tensile behaviour of individual fibre bundles in the human lumbar anulus fibrosus. Journal of biomechanics, 67, 24-31. https://doi.org/10.1016/j.jbiomech.2017.11.016

781 782 783

780

Robinson RA, Stokes RH (1949). Tables of osmotic and activity coefficients of electrolytes in aqueous solution at 25 C. Transactions of the Faraday Society, 45, 612-624. https://doi.org/10.1039/tf9494500612

785 786 787

788

784

Schollum ML, Robertson PA, Broom ND (2010). How age influences unravelling morphology of annular lamellae-a study of interfibre cohesivity in the lumbar disc. Journal of anatomy, 216(3), 310-319. https://doi.org/10.1111/j.1469-7580.2009.01197.x

789 790

791 Screen HR, Chhaya VH, Greenwald SE, Bader DL, Lee DA and Shelton JC (2006). The 792 influence of swelling and matrix degradation on the microstructural integrity of tendon. Acta 793 biomaterialia, 2(5), 505-513. https://doi.org/10.1016/j.actbio.2006.05.008

794

795 Shaw KM, Lewis G (1997). Tensile properties of human Achilles tendon. In Proceedings of the 796 1997 16 Southern Biomedical Engineering Conference (pp. 338-341). IEEE. 797 https://doi.org/10.1109/SBEC.1997.583304

- Shirazi-Adl SA, Shrivastava SC, Ahmed AM (1984). Stress analysis of the lumbar disc-body unit in compression. A three-dimensional nonlinear finite element study. Spine, 9(2), 120-134.
- 801 https://doi.org/10.1097/00007632-198403000-00003

- Skaggs DL and Weidenbaum M (1994). Regional variation in tensile properties and biomechanics composition of the human lumbar annulus fibrous. Spine, 9, 120-134.
- 805 https://doi.org/10.1097/00007632-199406000-00002

806

Spilker RL, Jakobs DM and Schultz AB (1986). Material constants for a finite element model of the intervertebral disk with a fiber composite annulus. Journal of biomechanical engineering, 108(1), 1-11. https://doi.org/10.1115/1.3138575

810

Sun W, Sacks MS, Scott MJ (2005). Effects of boundary conditions on the estimation of the planar biaxial mechanical properties of soft tissues. Journal of biomechanical engineering, 127(4), 709-715. https://doi.org/10.1115/1.1933931

814

Svensson RB, Smith ST, Moyer PJ, Magnusson SP (2018). Effects of maturation and advanced glycation on tensile mechanics of collagen fibrils from rat tail and Achilles tendons. Acta biomaterialia, 70, 270-280. https://doi.org/10.1016/j.actbio.2018.02.005

818

- Szczesny SE and Elliott DM (2014). Interfibrillar shear stress is the loading mechanism of collagen fibrils in tendon. Acta biomaterialia, 10(6), 2582-2590.
- 821 https://doi.org/10.1016/j.actbio.2014.01.032

822

- Szczesny SE, Fetchko KL, Dodge GR, Elliott DM (2017). Evidence that interfibrillar load transfer in tendon is supported by small diameter fibrils and not extrafibrillar tissue components. Journal of Orthopaedic Research, 35(10), 2127-2134.
- 826 https://doi.org/10.1002/jor.23517

827

- Urban JPG, Maroudas A (1979). The measurement of fixed charged density in the intervertebral disc. Biochimica et Biophysica Acta (BBA)-General Subjects, 586(1), 166-178.
- 830 https://doi.org/10.1016/0304-4165(79)90415-X

831

Vergari C, Mansfield J, Meakin JR, Winlove PC (2016). Lamellar and fibre bundle mechanics of the annulus fibrosus in bovine intervertebral disc. Acta biomaterialia, 37, 14-20. https://doi.org/10.1016/j.actbio.2016.04.002

835

- Wagner DR, Lotz JC (2004). Theoretical model and experimental results for the nonlinear elastic behavior of human annulus fibrosus. Journal of orthopaedic research, 22(4), 901-909.
- 838 https://doi.org/10.1016/j.orthres.2003.12.012

839

Wagner DR, Reiser KM, Lotz JC (2006). Glycation increases human annulus fibrosus stiffness in both experimental measurements and theoretical predictions. Journal of biomechanics, 39(6), 1021-1029. https://doi.org/10.1016/j.jbiomech.2005.02.013

- 844 Wang MC, Pins GD and Silver FH (1994). Collagen fibres with improved strength for the repair
- 845 of soft tissue injuries. Biomaterials, 15(7), 507-512. https://doi.org/10.1016/0142-
- 846 9612(94)90016-7

- 848 Werbner B, Zhou M, O'Connell GD (2017). A novel method for repeatable failure testing of annulus fibrosus. Journal of biomechanical engineering, 139(11), 111001.
- 849 850 https://doi.org/10.1115/1.4037855

851

- 852 Werbner B, Spack K and O'Connell GD (2019). Bovine annulus fibrosus hydration affects rate-853 dependent failure mechanics in tension. Journal of biomechanics, 89, 34-39.
- 854 https://doi.org/10.1016/j.jbiomech.2019.04.008

855

856 White AA, Panjabi MM (1990). Clinical biomechanics of the spine. Philadelphia, PA, 857 USALippincott.

858

859 Wu HC, Yao RF (1976). Mechanical behavior of the human annulus fibrosus. Journal of 860 biomechanics, 9(1), 1-7. https://doi.org/10.1016/0021-9290(76)90132-9

861

862 Wren TA, Yerby SA, Beaupré GS and Carter DR (2001). Mechanical properties of the human 863 achilles tendon. Clinical biomechanics, 16(3), 245-251. https://doi.org/10.1016/S0268-864 0033(00)00089-9

865

866 Zak M, Pezowicz C (2013). Spinal sections and regional variations in the mechanical properties 867 of the annulus fibrosus subjected to tensile loading. Acta of bioengineering and biomechanics, 15(1). https://doi.org/10.5277/abb130107 868

869

871

870 Zak M, Pezowicz C (2016). Analysis of the impact of the course of hydration on the mechanical properties of the annulus fibrosus of the intervertebral disc. European Spine Journal, 25(9), 2681-872 2690. https://doi.org/10.1007/s00586-016-4704-0

873

874 Zhou M, Bezci SE and O'Connell GD (2020). Multiscale composite model of fiber-reinforced 875 tissues with direct representation of sub-tissue properties. Biomechanics and modeling in 876 mechanobiology, 19, 745-749. https://doi.org/10.1007/s10237-019-01246-x

- 878 Zhou M, Werbner B and O'Connell G (2020). Historical review on combined experimental and
- 879 computational approaches for investigating annulus fibrosus mechanics. Journal of
- 880 Biomechanical Engineering. 142(3), 030802. https://doi.org/10.1115/1.4046186